Journal of Materials Chemistry C

ROYAL SOCIETY OF CHEMISTRY

PAPER

View Article Online
View Journal | View Issue

Cite this: J. Mater. Chem. C, 2024, 12, 16817

Artificial light harvesting gel based on saponification-triggered gelation of aggregation-induced emissive BODIHYs†

Durgendra Yadav,[a] Vishwa Deepak Singh,[b] Ashish Kumar Kushwaha,[a] Anjani Kumar[a] and Roop Shikha Singh *[a]

Received 25th April 2024,
Accepted 2nd September 2024

DOI: 10.1039/d4tc01694g

rsc.li/materials-c

The present work provides a detailed study on saponification-triggered gelation of ester-based BODIHYs (**B1** and **B2**) derived from ethyl 4-(2-(benzo[*d*]thiazol-2-yl(cyano)methylene)-hydrazinyl)-benzoate (**L1**) and diethyl 5-(2-(benzo[*d*]thiazol-2-yl(cyano)methylene)hydrazinyl)-isophthalate (**L2**). The ligands and BODIHYs display good emission in the solution and solid states. This study describes the gelation of BODIHYs for the first time, wherein stable gels $\mathbf{GL_2}$ and $\mathbf{GB_2}$ were prepared *via* saponification-triggered gelation of **L2** and **B2**, respectively. The gelation and optical properties of the ligands and BODIHYs were compared through single-crystal X-ray diffraction studies. This work further explores the prospect of artificial light harvesting (ALH) *via* fabrication of ALHSs in the solution {**B1**/rhodamine B (**RhB**) and **B2**/**RhB**} and gel states ($\mathbf{GB_2}$/**RhB**). It was observed that in the presence of **RhB**, the emission intensities of BODIHYs and the gel decreased but those of **RhB** increased. The significant overlapping between the absorption spectrum of **RhB** and emission spectra of aggregates/gel suggests the possibility of energy transfer *via* noncovalent interactions. In these systems, **B1**, **B2** and $\mathbf{GB_2}$ served as donors, whereas **RhB** served as an acceptor.

Introduction

The increasing demand for energy from natural resources emerging from the rising global population has caused a worldwide energy shortage.[1–3] The current energy crisis has necessitated a surge in sustainable alternative energy resources that could eventually reduce the reliance on fossil fuels.[4–6] Solar energy, the driving force behind photosynthesis in natural green plants and some photosynthetic bacteria, is the most sought-after renewable energy resource.[7,8] Harnessing solar energy to power chemical reactions through luminescent materials,[9] photocatalysis,[10,11] fluorescent sensors[12,13] and bioimaging[14] has drastically changed the renewable energy landscape. Inspired by nature, several artificial light harvesting systems (ALHSs) using porphyrin assemblage molecular polymers,[15–17] dendritic macromolecules,[18,19] organic gels,[20–22] nanocrystals,[23–25] coordination compounds,[26–28] *etc.* have been developed, which have opened a new avenue for mitigating global energy sustainability. The simulation of a natural photosynthetic apparatus is based on the incorporation and precise orientation of multiple donors and one acceptor, which would lead to the efficient utilization of solar energy through energy transfer between an excited state donor (D) and a proximal ground state acceptor (A) *via* a non-radiative Förster resonance energy transfer (FRET) process.[29,30] This implies that donor–acceptor spatial organization in supramolecular assemblies facilitated by non-covalent interaction can be categorically utilized for exploring energy transfer in ALHSs. In this context, supramolecular gelatinous materials show more potential than conventional solution based ALHSs owing to their stability as well as tighter and ordered arrangements of donor molecules.[31–33] The three-dimensional network of a gel can effectively avoid self-quenching of the excited state by preventing the proximity between acceptor molecules by providing a suitable distance. In recent years, the major focus of the researchers has been on the molecular self-assembly of small molecules to form low molecular weight gelators (LMWGs) considering their implementation in optoelectronics,[34] adhesive materials[35] and drug delivery.[36–38] The properties of LMWGs are usually fine-tuned by their design and molecular architecture by alternating noncovalent or weak interactions, including hydrogen bonding,[39] π–π stacking,[40] van der Waals,[41] dipole–dipole,[42] and electrostatic forces.[43] Despite the apparent advantages, ALHSs based on supramolecular LMWGs have attracted very little attention. Further, solid-state emission has become indispensable for the practical application of functionalized luminescent materials, which has led to a great surge in the exploration of

[a] Department of Chemistry, Institute of Science, Banaras Hindu University, Varanasi-221 005, UP, India. E-mail: roopshikha22singh@gmail.com
[b] Department of Chemistry, D.A.V. P.G. College, Gorakhpur-273001, UP, India

† Electronic supplementary information (ESI) available: ^{1}H, ^{13}C, ^{11}B, ^{19}F NMR, HRMS, Fluorescence spectra, theoretical studies and tables are provided. CCDC 2337969, 2337970, 2309327 and 2309328. For ESI and crystallographic data in CIF or other electronic format see DOI: https://doi.org/10.1039/d4tc01694g

aggregation-induced emission (AIE) materials.[44,45] The above-mentioned facts have led to an understanding that despite the challenges, the exploration of AIE supramolecular LMWGs is more conducive to the development of efficient ALHSs.[46]

To achieve the exigent demand of AIE in LMWGs, we focused our attention on boron difluoride ($-BF_2$) coordinated luminescent materials due to their potential applications in diverse areas, such as material chemistry,[47] biological chemistry[48] and optoelectronics.[49] Among these, boron dipyrromethene (BODIPY) emerges as an obvious choice; however, their applications are greatly limited by aggregation-caused quenching (ACQ) and small Stokes shift, which results in self-absorption of its fluorescence.[50] In this direction, Aprahamian and Gilroy *et al.* reported a new class of boron-difluoride (BF_2)–hydrazone complexes (BODIHYs) exhibiting solid-state luminescence and aggregation-induced emission (AIE).[51–55] The AIEgens display valuable photophysical properties with an increasing concentration or upon aggregation, as AIE alleviates close packing in the molecules *via* various pathways: conformational planarization, J-aggregate formation, *E*/*Z* isomerization, twisted intramolecular charge transfer (TICT), excited-state intramolecular proton transfer (ESIPT), and restriction of intramolecular motion (RIM).[56]

Therefore, to develop AIE-based LMWGs with efficient light harvesting ability, we design and synthesize two BODIHYs using a benzothiazole–hydrazone chelating platform. As it is well known that the peripherally substituted ester(s) are suitable for gelation[57] and the phenyl ring may favour the process by increasing the planar π-interactions, the gelation of the BODIHYs has been achieved by incorporating several ester substituents ($-COOC_2H_5$) on the phenyl ring. Herein, we describe the synthesis thorough characterizations and photophysical properties of BODIHYs (**B1** and **B2**) and their corresponding ligands ethyl 4-(2-(benzo[*d*]thiazol-2-yl(cyano)methylene)-hydrazinyl)-benzoate (**L1**) and diethyl 5-(2-(benzo[*d*]thiazol-2-yl(cyano)methylene)hydrazinyl)-isophthalate (**L2**). **B1**, **B2** and **L1** are AIE active. Gelation was triggered in **B2** and **L2** by saponification through NaOH. ALHSs in an aqueous and organic medium are constructed utilizing these assemblies as donors, while rhodamine dye (**RhB**) is used as an acceptor. To the best of our knowledge, this is the first report dealing with gelation in BODIHYs produced by saponification and light harvesting applications.

Experimental section

Syntheses

Synthesis of A1 and A2. Anilines benzocaine (**A1**) and diethyl-5-aminoisophthalate (DAE; **A2**) were synthesized following the literature methods.[58,59]

Synthesis of L1. Benzocaine **A1** (5.73 mmol) was dissolved in a mixture of conc. HCl (37%, 7.0 mL) and ice-cold water (15 mL). The resulting solution was stirred for 15 min. and subsequently diazotized using sodium nitrite (6.87 mmol) at 0–5 °C. The light cream solution thus obtained was stirred for another 60 min, and the resulting diazonium salt solution was treated dropwise with a suspension of 2-benzothiazole-acetonitrile (5.73 mmol) and sodium acetate (34.3 mmol) in an ice-cold mixture of ethanol (~35 mL) and water (~10 mL). The resulting reaction mixture was stirred overnight at room temperature. The yellow precipitate thus obtained was filtered, dissolved in DCM and finally washed with saturated sodium bicarbonate solution, followed by brine and dried over $MgSO_4$. The crude product was purified by silica gel column chromatography using 1 : 8 (ethyl acetate/hexane) as an eluent to produce **L1** as a yellow powder (758 mg). ^{1}H NMR (500 MHz, $CDCl_3$): δ = 14.41 (s, 1H, N-*H*), 8.09 (d, J = 6 Hz, 3H, *H*3 and *H*5), 7.99 (d, J = 8 Hz, 1H, *H*8), 7.60 (t, J = 6.5 Hz, 1H, *H*7), 7.52 (t, J = 8 Hz, 1H, *H*6), 7.46 (d, J = 8 Hz, 2H, *H*4), 4.40–4.35 (q, J = 6.5 Hz, 2H, *H*2), 1.40 ppm (t, J = 6.5 Hz, 3H, *H*1). ^{13}C NMR (125 MHz, $CDCl_3$): δ = 166.0, 159.6, 152.6, 145.1, 133.4, 131.4, 127.5, 127.0, 126.8, 123.2, 122.1, 116.2, 115.1, 108.9, 61.1, 14.4 ppm. HRMS (*m*/*z* calcd for $C_{18}H_{14}N_4O_2S$ [M]): 350.0837; found $[M + H]^+$: 351.1029.

Synthesis of L2. This compound was synthesized following the above procedure for **L1** using DAE (**A2**). It was isolated as a dark yellow crystalline powder (815 mg). ^{1}H NMR (500 MHz, $CDCl_3$): δ = 14.43 (s, 1H, N-*H*), 8.44 (s, 1H, *H*3), 8.25 (s, 2H, *H*4), 8.14 (d, J = 8 Hz, 1H, *H*5), 7.98 (d, J = 10 Hz, 1H, *H*8), 7.62 (t, J = 7 Hz, 1H, *H*7), 7.52 (t, J = 8 Hz, 1H, *H*6) 4.47–4.43 (q, J = 6.5 Hz, 2H, *H*2), 1.45 ppm (t, J = 6.5 Hz, 3H, *H*1). ^{13}C (125 MHz, $CDCl_3$): δ = 165.4, 159.7, 152.7, 142.3, 133.3, 132.6, 127.5, 127.0, 126.6, 123.3, 122.0, 120.3, 116.2, 108.8, 61.8, 14.4 ppm. HRMS (*m*/*z* calcd for $C_{21}H_{18}N_4O_4S$ [M]): 422.0824; found $[M + H]^+$: 423.1266.

Synthesis of B1. Ligand **L1** [(*Z*)-ethyl-4-m(2-(benzo[*d*]thiazol-2-yl(cyano)methyl-ene)hydrazinyl)benzoate] (2.85 mmol) was dissolved in dichloromethane, and a solution of *N*,*N*-diisopropylethylamine (DIPEA, 2.9 mL) and $BF_3{\cdot}OEt_2$ (4.5 mL) was added dropwise to the resulting reaction mixture for 1 h. The reaction mixture was stirred overnight and subsequently quenched by adding 20 mL of water. The organic layer was separated and washed twice with water and brine and finally dried over $MgSO_4$. It was concentrated to dryness on a rotatory evaporator, and the crude product thus obtained was subjected to silica gel column chromatography using 4 : 1 hexane/ethyl acetate as an eluent to give **B1** as a yellow crystalline powder (548 mg). ^{1}H NMR (500 MHz, $CDCl_3$): δ = 8.32 (d, J = 8 Hz, 1H, *H*5), 8.11 (d, J = 9.5 Hz, 2H, *H*3), 7.90 (d, J = 8 Hz, 1H, *H*8), 7.89 (d, J = 8 Hz, 2H, *H*4), 7.74 (t, J = 8 Hz, 1H, *H*7), 7.66 (t, J = 7 Hz, 1H, *H*6) 4.41–4.36 (q, J = 6.5 Hz, 2H, *H*2), 1.40 ppm (t, J = 6.5 Hz, 3H, *H*1). ^{13}C NMR (125 MHz, $CDCl_3$): δ = 166.0, 157.7, 147.7, 142.7, 130.7, 129.6, 129.1, 128.4, 122.8, 120.6, 120.3, 114.3, 61.2, 14.4 ppm. ^{11}B NMR (160.4 MHz, $CDCl_3$): δ = 0.48, 0.29, 0.09 ppm (t, 1B). ^{19}F NMR (470.6 MHz, $CDCl_3$): δ = −129.3, −129.2, −129.2, −129.1 ppm (q, 2F). HRMS (*m*/*z* calcd for $C_{18}H_{13}BF_2N_4O_2S$ [M]): 398.0820; found $[M + H]^+$: 399.1034.

Synthesis of B2. It was synthesized following the above procedure for **B1** using **L2** [(*Z*)-diethyl 5-(2-(benzo[*d*]thiazol-2-yl(cyano)methylene)hydrazinyl)isophthalate] as a ligand. **B2** was obtained as a brown crystalline powder (498 mg). ^{1}H NMR (500 MHz, $CDCl_3$): δ = 8.65 (s, 2H, *H*4), 8.63 (s, 1H, *H*3), 8.35 (d, J = 8.0 Hz, 1H, *H*5), 8.00 (d, J = 8.5 Hz, 1H, *H*8), 7.76 (d, J = 8.5 Hz, 1H, *H*7), 7.67 (d, J = 8.0 Hz, 1H, *H*6), 4.44 (q, J = 8.0 Hz, 4H, *H*2), 1.44 ppm (t, J = 8.0 Hz, 6H, *H*1). ^{13}C NMR

(125 MHz, $CDCl_3$): δ = 165.2, 157.8, 144.8, 142.7, 132.2, 129.6, 129.3, 129.2, 128.5, 125.9, 122.8, 120.3, 114.3, 61.7, 14.4 ppm. ^{11}B NMR (160.4 MHz, $CDCl_3$): δ = 0.48, 0.28, 0.09 ppm (t, 1B). ^{19}F NMR (470.6 MHz, $CDCl_3$): δ = −129.3, −129.3, −129.2, −129.2 ppm (q, 2F). HRMS (*m*/*z* calcd for $C_{21}H_{17}BF_2N_4O_4S$ [M]): 470.1032; found $[M + H]^+$: 471.1269.

Results and discussion

Syntheses and characterizations

Syntheses of the hydrazones **L1–L2** and their $-BF_2$ complexes, BODIHYs **B1–B2**, are achieved by following the literature procedures and using $BF_3{\cdot}Et_2O$ in the presence of *N*,*N*-diisopropylethylamine (DIPEA). A simple scheme showing the synthesis of the ligands (**L1–L2**) and BODIHYs (**B1–B2**) is depicted in Scheme 1. The ligands and BODIHYs under investigation are air-stable, non-hygroscopic solids, soluble in common organic solvents, such as diethyl ether, petroleum ether, hexane, acetonitrile, methanol, ethanol, acetone, dichloromethane, chloroform, dimethylformamide, dimethyl-sulfoxide, and insoluble in water. Characterization of these compounds is performed by acquiring NMR (^1H, ^{13}C, ^{11}B, ^{19}F), HRMS, electronic absorption and emission spectral data (Fig. 1 and Fig. S1–S8, ESI†). ^1H, ^{13}C, ^{11}B, and ^{19}F spectral data are presented in the Experimental section, and spectra are shown through Fig. S1–S6 (ESI†).

The N–H protons for **L1** and **L2** resonated as a singlet at δ 14.41 and 14.43 ppm, while aromatic protons appeared as broad multiplets in the range of $\delta \sim$ 8.44–7.24 ppm. In addition, methylene and methyl protons appeared as a quartet and a triplet, respectively, at δ 4.38 (2H), 1.40 ppm (3H) in **L1** and 4.44 (4H), 1.45 (6H) in **L2**. After the formation of BODIHYs, the N–H proton disappeared, and a broad multiplet of aromatic protons resonated in the downfield region in the range of $\delta \sim$ 7.64–8.33 (**B1**) and 7.65–8.65 ppm (**B2**). ^{13}C NMR spectroscopic data for the ligand (**L1–L2**) and BODIHYs (**B1–B2**) further supported their formation and proposed structures. HRMS strongly supported the formation of the compounds: **L1**, **L2**, **B1** and **B2**. As expected in their mass spectra, the compounds under investigation displayed molecular ion peaks at *m*/*z* $[M + H]^+$: 351.1029, 423.1266, 399.1034 and 471.1269 (Fig. S7 and S8, ESI†), further confirming their respective formulations.

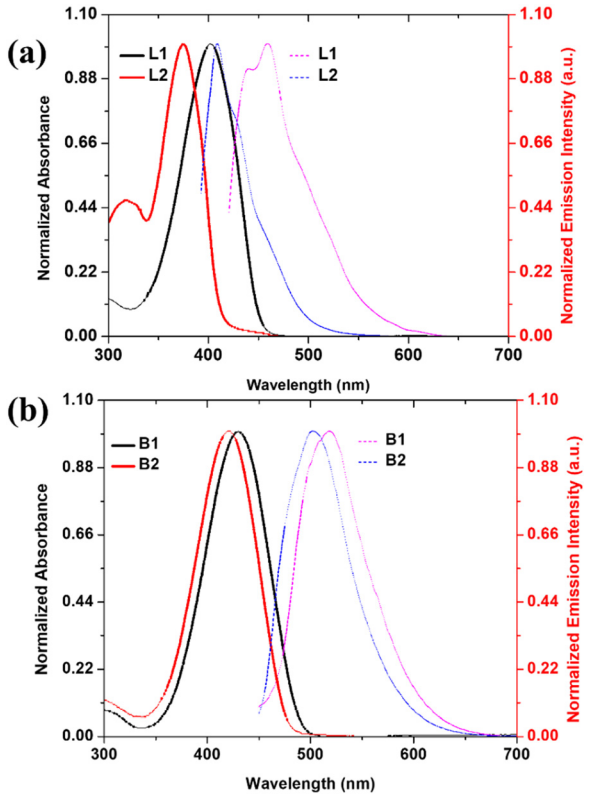

Fig. 1 Normalized UV-Vis absorption and emission spectra of ligands (**L1–L2**) (a) and BODIHYs (**B1–B2**) (b) in THF (*c*, 5.0 × 10^{-5} M).

Photophysical studies

The photophysical behaviour of hydrazone ligands (**L1–L2**) and BODIHYs (**B1–B2**) has been examined in dilute solutions through UV/Vis and photoluminescence studies. Ligands under study displayed absorptions (λ_{abs}) at 403 (**L1**) and 392 nm (**L2**) (THF; *c*, 5.0 × 10^{-5} M) due to intramolecular charge transfer (ICT).[60] However, the intense ICT absorption bands in **B1** and **B2** were observable at 428 and 421 nm, respectively. Further, when excited at 403 (**L1**) and 392 nm (**L2**), they showed emission maxima at 459 and 435 nm with a Stokes shift (SS) of ∼3026 and ∼2521 cm^{-1}, respectively. The solution fluorescence quantum yield (Φ_f) of **L1** and **L2** were found to be 7.6 and 35.3%, respectively. Upon excitation, **B1** showed emission

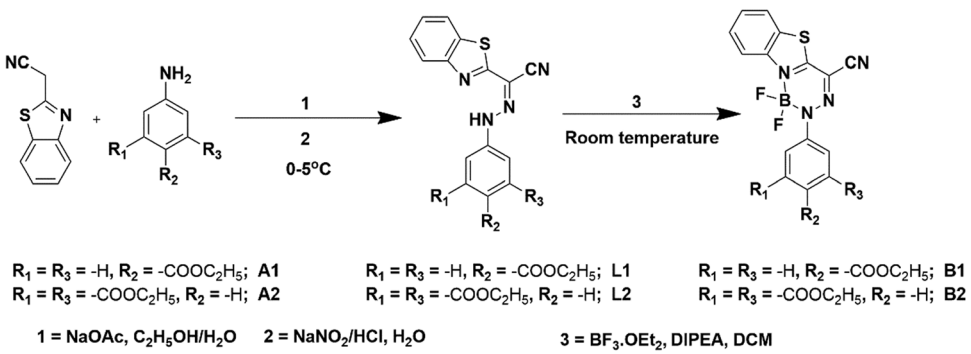

Scheme 1 Synthesis of ligands (**L1–L2**) and BODIHYs (**B1–B2**).

maxima at 519 with Stokes shift (SS) and Φ_f of ~3955 cm^{-1} and 4.5%, respectively. However, **B2** exhibited emission maxima at 503 nm with Stokes shift and Φ_f of ~3832 cm^{-1} and 8.3%, respectively (Fig. 1). Apparently, blue-shifted absorption and emission as well as higher Φ_f for **L2** and **B2** in solution may be attributed to the presence of one additional electron withdrawing ester group ($-COOC_2H_5$), which weakens the ICT character in the ground and excited states.[61]

In their solid-state (powder) emission profile, upon excitation at 403 and 392 nm, **L1** and **L2** both showed a broad band (500–650 nm) with the maxima centred at 548 (with a shoulder at ~576 nm) and 571 nm, respectively. **B1** and **B2** showed broad bands (475–700 nm) upon excitation at ~428 and 421 nm, with maxima centred at 586 and 571 nm, respectively (Fig. S9, ESI†). Similarly, solution **B2** displayed a blue-shifted emission maximum relative to solution **B1**. The red-shifted emission wavelengths of **B1** and **B2** in the solid state compared to their solution state can be attributed to increased intermolecular interactions in the solid state. Further, the observation of ICT bands in the absorption spectra and broad solubility range of **B1–B2** compounds in common organic solvents, such as hexane, benzene, toluene, 1,4-dioxane, $CHCl_3$, tetrahydrofuran (THF), CH_2Cl_2, DMF, CH_3CN, and CH_3OH, prompted us to examine the dependence of the excited state on solvent polarity. Going from non-polar (hexane; f = 0.0) to polar (methanol; f = 0.309) solvents, the emission band displayed significant broadening with a decrease in emission intensities. The typical bathochromic shift of the emission maxima in polar solvents ($\Delta\lambda$ = 8 nm, **B1** and 13 nm, **B2**) suggested the involvement of the ICT state for BODIHY complexes (**B1** and **B2**) (Fig. S10, ESI†).

Aggregation-induced emission (AIE)

The excellent solid-state emission of ligands and BODIHYs is anticipated to be accompanied by the AIE attribute. To validate AIE, the absorption and emission behaviour of the ligand **L1–L2** and BODIHY **B1–B2** are investigated in THF/water binary mixture. In their absorption spectra, the ligands (**L1–L2**) did not show any major changes up to water fraction (f_w) 70%, but as f_w approached 80%, a bathochromic shift was observed along with a prominent level off tail, indicating aggregate formation (Fig. S11, ESI†). Variation of water fraction in the range 80–99% caused a red shift (403 to 418, **L1**; 392 to 401 nm, **L2**) in the absorption band with quenched absorbance. Further, it was observed that the ligands (**L1–L2**) displayed analogous emission features toward variation in the water fraction. At f_w 0%, **L1** displayed emission maxima (λ_{max}) at 459 nm, which shifted to 505 nm at f_w 90% with ~9-fold emission enhancement. Moreover, **L2** at f_w 0% showed λ_{max} at 435 nm, which red shifted to 537 nm at f_w 99% along with significant emission quenching (Fig. S12, ESI†).

Further, in their absorption spectra, both BODIHYs (**B1–B2**) showed insignificant changes of up to f_w 70%. However, as f_w approached 80%, a bathochromic shift was observable along

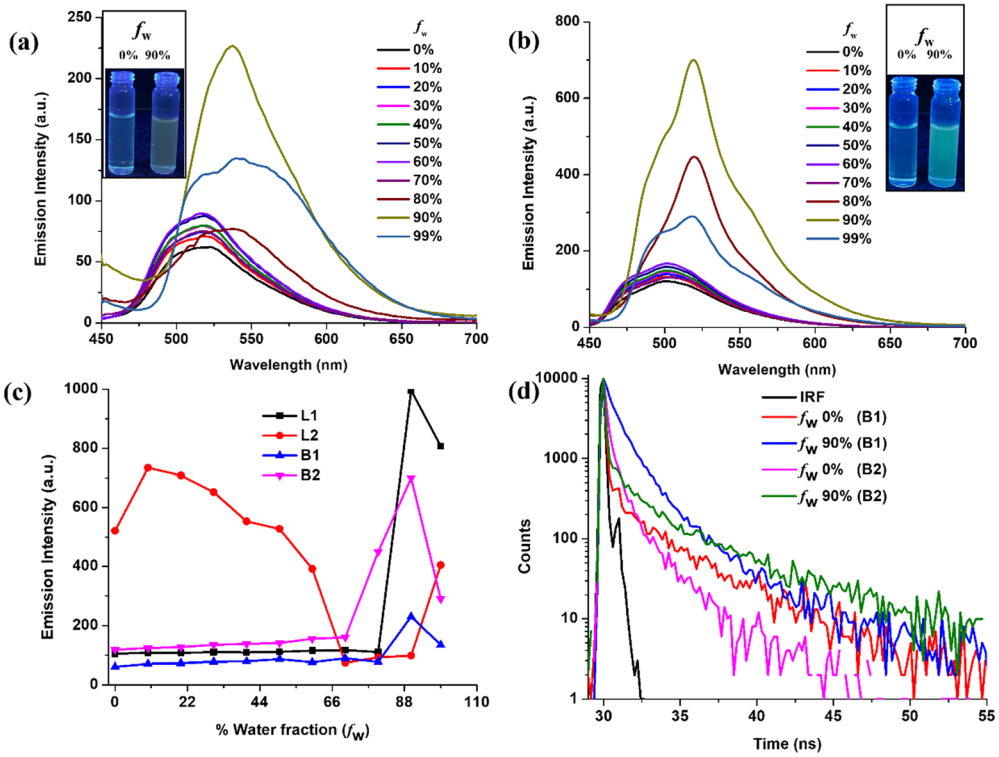

Fig. 2 Emission spectra of **B1** (a) and **B2** (b) in THF/water mixture with varying water fractions (*c*, 5.0 × 10^{-5} M); (c) plot between emission intensity and THF/water fractions; and (d) a logarithmic view of time-resolved fluorescence of **B1** and **B2** (a) in THF (f_w = 0%) and THF/water (f_w = 90%) (*c*, 5.0 × 10^{-5} M).

with the broadening of the absorption band, which in turn indicated the onset of aggregation (Fig. S13, ESI†). Variation of the water fraction in the range of 80–99% led to a red shift (432–445, **B1**; 421–432 nm, **B2**) for the absorption band with quenched absorbance. In a large excess of water (f_w 99%), they exhibited bathochromically shifted absorption bands relative to THF solution (f_w 0%) with a level off tail due to Mie scattering for the aggregate suspension. The emissive behaviour of ensuing aggregates was further investigated by recording the emission profile in an analogous solvent system.

As depicted in Fig. 2, luminophores **B1** and **B2** showed weak emission in the dilute (THF) solution (f_w 0%) at 519 and 503 nm, respectively. The gradual addition of water up to f_w 70% caused insignificant changes in their emission behaviour; however, when the f_w reached 90%, **B1** and **B2** exhibited appreciable emission enhancement (∼5- and 8-fold). Interestingly, these luminophores showed emission quenching at f_w 99% accompanied by a bathochromic shift to 537 (**B1**) and 520 nm (**B2**), which can be attributed to decreased solubility and precipitation. From the above observations, it can be surmised that ligand **L2** displays typical ACQ behaviour with an obvious red shift. However, ligand **L1** and BODIHYs (**B1** and **B2**) displayed fluorescence enhancement upon aggregation. Thus, these can be classified as AIEgens. These observations have further been supported by DLS studies (Fig. S14a, ESI†). As expected, at f_w 90%, the average size of nanoaggregates is found to be ∼200 (**L1**), 500 (**B1**) and 150 nm (**B2**). Further, the Tyndall effect for **L1**, **B1** and **B2** in THF/water (f_w 0% and 90%) validated the formation of aggregates (Fig. S14b, ESI†).[62]

The morphology of aggregates was analysed by SEM studies on **L1**, **B1** and **B2** at f_w 90%. With an increasing water gradient, intermolecular interactions in **L1**, **B1** and **B2** favour the formation of roughly spherical aggregates (Fig. S15, ESI†). Further, it is well known that restriction of intramolecular rotations (RIR) caused by aggregation is one of the most prominent factors behind the emission enhancement in AIEgens.[63] Therefore, the possible mechanism for AIE is investigated by evaluating the viscosity sensitivities of **L1**, **B1** and **B2**. In this regard, emission spectra of **L1**, **B1** and **B2** are obtained in a mixture of CH_3OH/glycerol (c, 5.0×10^{-5} M) with varying glycerol fractions.

As shown in Fig. S16 (ESI†) emission intensity for **L1** (∼6 times), **B1** (∼16 times) and **B2** (∼15 times) enhanced with increasing glycerol fraction accompanied by a small bathochromic shift in the position of emission maxima (465–490 nm; **L1**, 522 to 529 nm; **B1** and 502–507 nm; **B2**). Restriction of active intramolecular rotations in viscous solvent resulted in the rigidification of luminophores, thereby impeding the creation of a dark state by blocking the non-radiative decay channels, which further led to enhanced emission.

Additionally, AIE was verified through fluorescence lifetime measurements of THF/water solutions of **L1**, **B1** and **B2** at varying water fractions. It was observed that the lifetime increased from 0.20 (f_w = 50%), 0.08 and 0.02 (f_w = 0%) to 0.77, 0.87 and 0.22 ns (f_w = 90%) for **L1**, **B1** and **B2**, respectively, supporting the emission enhancement upon aggregation (Fig. 2d and Fig. S17, ESI†). The longer lifetime in the aggregated state can be attributed to the lowering of the non-radiative decay through restricted molecular rotations. From the above results, it can be concluded that RIR is responsible for AIE in these systems.

Single-crystal X-ray

It is believed that structural and packing analyses of the luminophores through single-crystal X-ray crystallography may provide detailed information about the intermolecular interactions, which are the driving forces toward the creation of hierarchical supramolecular structures. We further presumed that the gelation process and corresponding photophysical behaviour may be a cumulative outcome of the self-assembly process in crystallization. The single-crystal structures of the ligands (**L1** and **L2**) BODIHYs (**B1** and **B2**) are unambiguously authenticated by X-ray single-crystal studies, and ORTEP views are shown in Fig. 3. Details about data collection, solution and refinement are presented in Table S1 (ESI†).

From the crystal structure of **L1** and **L2**, it is clear that the former has no π–π interactions while the latter has a single π–π interaction (3.337 Å) (Fig. S18, ESI†). The absence of π–π interaction in **L1** can prevent the formation of closely packed structures and lead to AIE, unlike ACQ in **L2**, which shows π–π interactions. Interestingly, **L1** forms a 'V'-shape crystal packing pattern due to short interaction between O and H (2.719 Å). Similarly, the short interaction between N and H (2.640 Å) forms a dimeric structure in **L2** (Fig. S18, ESI†). **B1** forms two antiparallel chains with head-to-tail and head-to-head arrangement *via* π–π interactions. Two π–π interactions are illustrated in Fig. 4: one between benzene rings of adjacent benzothiazole moieties (3.359 Å) and the other between carbons of the methylene group and ester moiety (3.398 Å). However, **B2** was arranged in a "classical" slipped stacked manner with π–π interaction (3.395 Å) favouring J-aggregation (Fig. 4).

Interestingly, **B1** has a nearly planar structure, while in **B2**, the BODIHY core is at 27.52° with the diethyl isophthalate core. This loss of planarity might prevent the very close packing of

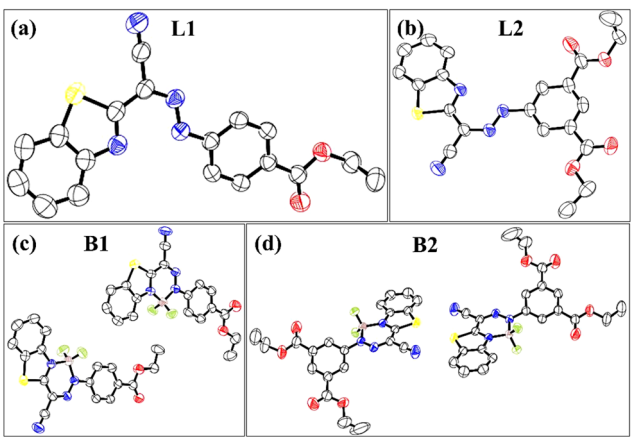

Fig. 3 ORTEP views of **L1** (a), **L2** (b), **B1** (c) and **B2** (d) at 50% ellipsoidal probability (H atoms are omitted for clarity).

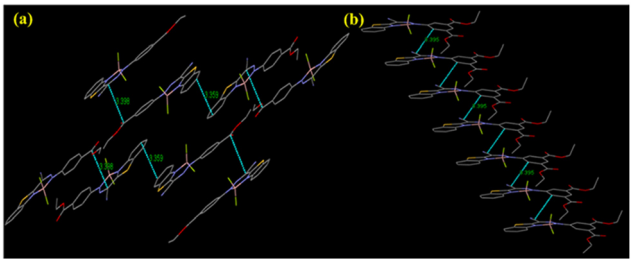

Fig. 4 Crystal packing in **B1** (a) and **B2** (b) *via* π–π interactions.

molecules in nanoaggregates and could be responsible for the greater emission enhancement of **B2** in an aggregated state. Further, the selected crystallographic parameters (bond angles and bond lengths) and important short interactions for **B1** and **B2** are presented in Tables S2–S4 (ESI†).

Gelation

Because an increase in dipole moment is critical for gelation, we attempted the saponification typically employed for the hydrolysis of fatty esters into $-COO^{-}Na^{+}/-K^{+}$ salts in the presence of a base (NaOH or KOH) to create polar groups with slight modification. It was found that a 10 mM solution of **L1** and **B1** in $CHCl_3$ instantly led to yellow colour gelatinous suspensions $\mathbf{GL_1}$ and $\mathbf{GB_1}$, respectively, in the presence of a methanolic solution of NaOH (Fig. S21 and S22, ESI†). However, ligand **L2** and BODIHY **B2** formed a stable gel under similar conditions, which was further confirmed by applying the inverted vial method ($\mathbf{GL_2}$ and $\mathbf{GB_2}$) (based on creating a compact gel in the minimum time, Fig. 5a and e). The weak nature of $\mathbf{GL_1}$ and $\mathbf{GB_1}$ compared to $\mathbf{GL_2}$ and $\mathbf{GB_2}$, respectively, is due to the number of peripheral ester groups present on the benzene ring (**1** in **L1** and **B1** while **2** in **L2** and **B2**), which are hydrolysed to carboxylate salts that facilitate gelation through π–π stacking and short intermolecular interactions.

Owing to the presence of two ester groups on **L2** and **B2**, saponification may create a mixture of Na^{+}-salts. Therefore, it is optimized by varying the ratios of **L2** and **B2** *versus* NaOH. In this context, we evaluated the photophysical behaviour of **L2** and **B2** in the presence of NaOH. As shown in Fig. 1, the UV/Vis spectra of **L2** and **B2** possessed prominent peaks at 393 and 421 nm, respectively. Upon the gradual addition of NaOH, **L2** exhibited a significant bathochromic shift accompanied by the emergence of a new band at 453 nm, while **B2** showed a gradual decrease in absorption with a small red shift (421–430 nm). Similarly, in fluorescence titration studies, **L2** and **B2** (c, 1×10^{-2} M) showed emission bands at 437 and 508 nm, respectively (Fig. S23, ESI†). The gradual addition of NaOH with a limit of quantification of 1.0 to 3.2 equiv. (**L2**) and 1.0 to 2.8 equiv. (**B2**) led to a decrease in florescence intensity with a red shift ($\Delta\lambda$, 40 and 10 nm). These changes clearly indicate the ratiometric conversion of the esters to carboxylates, leading to the formation of $\mathbf{L2} \rightarrow \mathbf{GL_2}$ and $\mathbf{B2} \rightarrow \mathbf{GB_2}$ through J-aggregation. The gelation was also scrutinized using other common solvents, and the resulting data are presented in Table S5 (ESI†).

Further, the morphological characteristics of gels $\mathbf{GL_2}$ and $\mathbf{GB_2}$ were investigated by atomic force, scanning electron and transmission electron microscopy (AFM, SEM and TEM). AFM analyses confirmed the interconnected fibrous morphology of $\mathbf{GL_2}$ (Fig. 5b) while numerous directional fibres were present in $\mathbf{GB_2}$ (Fig. 5f). SEM analyses further attested to the results obtained from AFM studies (Fig. 5c and g). In addition, TEM images showed significant interactions among the fibres in $\mathbf{GL_2}$ and $\mathbf{GB_2}$, which confirmed that they are involved in the creation of the gel fibres (Fig. 5d and h). The mechanical strength of the gel was characterized by its viscoelastic character and was measured by dynamic rheology. The storage (G') and loss (G'') moduli are measured as functions of shear stress (τ), oscillation strain (γ) and angular frequency (ω). The results revealed that the magnitude of G' is higher than that of G'' by an order of

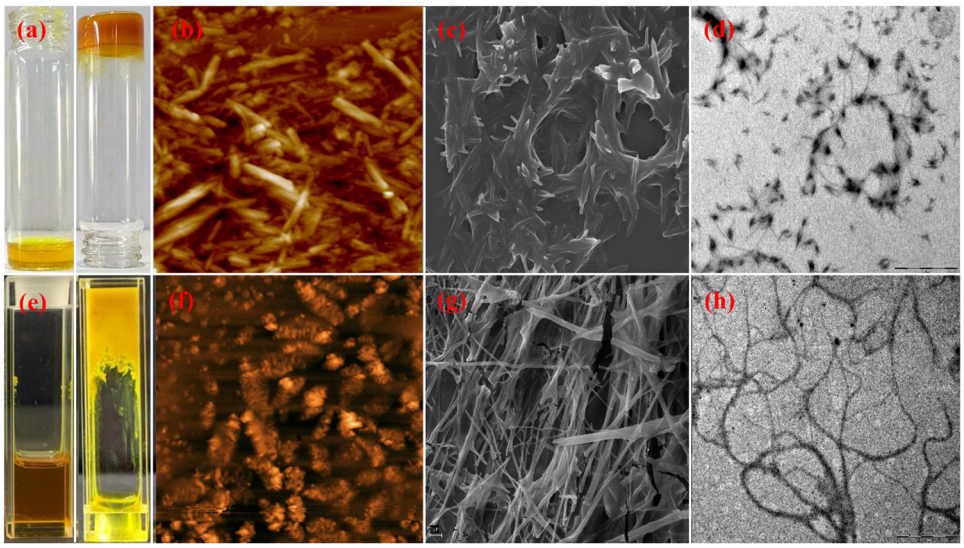

Fig. 5 (a) **L2** and gel $\mathbf{GL_2}$ in an inverted vial. (b) AFM, (c) SEM, and (d) TEM for $\mathbf{GL_2}$, (e) **B2** and $\mathbf{GB_2}$ in the inverted vial. (f) AFM, (g) SEM and (h) TEM for $\mathbf{GB_2}$.

magnitude up to a certain range of yield stress, showing a true gel nature. The linear viscoelastic (LVE) region is determined by the amplitude sweep of G' and G''.

In the present work, the $\mathbf{GL_2}$ and $\mathbf{GB_2}$ materials show a fair stretch of the LVE region and it is revealed by the frequency sweep measurements at the suggested strains (from amplitude sweep experiments) that $G' > G''$ is maintained throughout along with $\Delta(G' \sim G'')$ of 1 order (Fig. S24, ESI†).[64] The information regarding structural transformation during the gelation process is collected by ^{1}H-NMR titration of **L2** and **B2** (0.02 M) in $CDCl_3$ with 2.0 M NaOH in CD_3OD (Fig. S25 and S26, ESI†). Upon the gradual addition of NaOH, the loss of the ester group ($-CH_2CH_3$: 4H, δ = 4.45; 6H, 1.44 ppm) proton signals were observed. Simultaneously, there is an emergence of two new peaks at δ = 3.70, 1.25 ppm (**L2**) and 3.38, 1.26 ppm (**B2**) assignable to the free ethyl group ($-CH_2CH_3$). Interestingly, the N–H of **L2** at 14.5 ppm also disappeared with the addition of the base.

This conversion is also substantiated by the HRMS of $\mathbf{GL_2}$ and $\mathbf{GB_2}$ and the presence of suitable molecular ion peaks as well as their isotopic patterns, which matches well with the simulated one (Fig. S27 and S28, ESI†).

Additionally, to correlate the relative gelation efficiencies, centroid–centroid distances (ccds) between the planar rings involved in π–π stacking are investigated. The absence of π–π interactions in **L1** relative to that in **L2** can be associated with poor gelation efficiency of **L1** over **L2** (Fig. S18, ESI†). Further, from the crystal structure, it is observed that **B1** and **B2** are involved in significant intermolecular π-stacking interactions with ccds of 7.998 and 4.712 Å, respectively, between the 6-membered difluoroboron ring (Fig. S29, ESI†). Interestingly, the planar diethyl isophthalate rings involved in π-stacking are arranged in such a manner that they are aligned in one direction in **B2** and opposite to each other in **B1**. From the above observations, it can be surmised that smaller ccd and face-to-face positioning of diethyl isophthalate rings in **B2** might lead to a greater extent of π-interactions and consequently higher gelation efficiency in **B2** compared to **B1** through saponification.

Density function theory (DFT)

For a better understanding of photophysical behaviour and rationalization of the gelation mechanism, theoretical calculations are performed for ligands, BODIHYs and their saponified gels. The frontier molecular orbitals of ligands (**L1–L2**) and BODIHYs (**B1–B2**) are shown in Fig. 6 and Fig. S30 (ESI†). Theoretical studies have shown that the HOMO and LUMO of ligands extend mainly over the entire molecule, but the molecular orbital localization differs. This can be observed specifically at the benzene ring (directly attached to ester moiety), where the orbital accumulates around the carbon–carbon double bond at the HOMO state, whereas it is localized over the carbon–carbon single bond at the LUMO state, indicating conjugation within the molecule.[65] The band gap between the HOMO (−2.61, **L1**; −2.49 eV, **L2**) and LUMO (−6.02, **L1**; −6.01 eV, **L2**) for the ligands are 3.41 and 3.52 eV, respectively. However, in both the

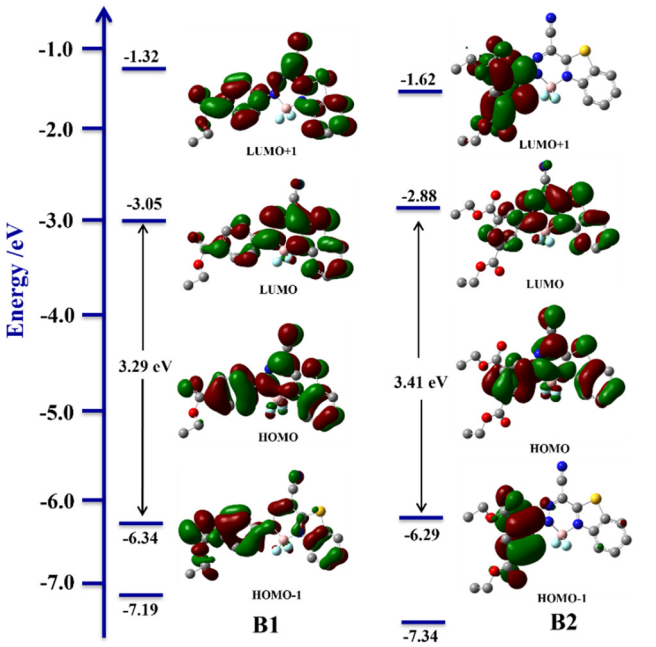

Fig. 6 Selected ground state molecular orbitals of **B1** and **B2** obtained from DFT calculations.

BODIHYs, HOMO−1, HOMO, LUMO and LUMO+1 are localized over phenyl and benzothiazole units. The band gaps between the HOMO (−6.34, **B1**; −6.29 eV, **B2**) and LUMO (−3.05, **B1**; −2.88 eV, **B2**) for these molecules are 3.29 and 3.41 eV, respectively. The larger band gap between molecular orbitals is attributed to the presence of two electron withdrawing substituents ($-COOC_2H_5$) in **L2** and **B2**, which further supports their blue-shifted absorption band relative to **L1** and **B1** (Fig. 1).

Further, experimental UV/Vis spectra are compared to those from TD-DFT (Fig. S31 and S32, ESI†). For ligands and BODIHYs, the major transition bands originated due to HOMO → LUMO (88%, **L1**; 85%, **L2**; 87%, **B1**; 88%, **B2**) transition (Table S6, ESI†). Thus, the overall theoretical results validated those obtained from the experimental measurements.

Furthermore, the comparison of DFT-optimized structures of saponified products $\mathbf{GL_1}$–$\mathbf{GL_2}$ and $\mathbf{GB_1}$–$\mathbf{GB_2}$ is performed (Fig. S30 and S33, ESI†). The HOMO and LUMO of $\mathbf{GL_1}$ and $\mathbf{GL_2}$ have a distribution similar to that of the ligands, while in the case of $\mathbf{GB_1}$ and $\mathbf{GB_2}$, similar electron densities are observed in HOMOs. However, in LUMOs, the electron densities are predominantly localized over phenyl and benzothiazole–BF_2 units in $\mathbf{GB_2}$, unlike in $\mathbf{GB_1}$.

As it is well known that an increase in the dipole moment is crucial for saponification-triggered gelation,[57] DFT calculations revealed an increase in the dipole moment from 6.85 → 10.39 (**L2** → $\mathbf{GL_2}$) and 4.58 → 7.13 Debye (**B2** → $\mathbf{GB_2}$) due to the $-COO^-Na^+$ moiety. Further, it is found that $\mathbf{GB_2}$ (7.13 Debye) has a higher dipole moment than $\mathbf{GB_1}$ (6.63), which in turn suggests the superior gelation efficiency of $\mathbf{GB_2}$. Notably, these saponified structures of BODIHYs have two planes in which one plane contains a benzothiazole moiety and the other has an isophthalate ring and Na^+ ion. In both cases, Na^+ ion is

expected to be involved in significant interactions with the first plane, which provides strong evidence of the dominant cation–π interaction in **GB_2** (1.657 and 4.053 Å) compared to **GB_1** (1.496 Å) (Fig. S34, ESI†).

Artificial light harvesting systems (ALHSs)

Red fluorescent rhodamine B (**RhB**) dye has strong absorption in the visible region at 556 nm and emission at 580 nm, making it extensively used in fluorescent studies.[66] Both luminophores (**B1** and **B2**) showed strong broad AIE emissions in aqueous solution (f_w = 90%) at 537 and 519 nm, respectively. It is apparent that there is a significant overlap between the emission spectra of aggregates of **B1** and **B2** and the absorption spectrum of RhB, which satisfies one of the most important criteria for FRET between donor and acceptor moieties and construction of ALH assemblies (Fig. 7 and Fig. S35, ESI†). It is worth mentioning that **L1** and **L2** fail to show FRET when employed as donors against RhB acceptors in ALH assemblies. This is due to poor spectral overlap between the emission of **L1** and **L2** and the absorption of RhB. Apparently, the incorporation of $-BF_2$ moiety in hydrazone ligands leads to red-shifted emission and increases the possibility of spectral overlap.

In this direction, aggregates of **B1** and **B2** were employed for the construction of ALH, wherein **B1** and **B2** act as donors while **RhB** acts as an acceptor. Upon gradual addition of **RhB** into the aggregate of **B1** (f_w = 90%), the emission intensity of **B1** quenched at λ_{em} = 537 nm with the synchronous appearance of a new emission at λ_{em} = 583 nm upon excitation at λ_{ex} = 428 nm. Furthermore, on varying the molar ratio of the donor : acceptor (D : A) from 250 : 1 to 27 : 1, the ~5-fold emission enhancement is observed at 583 nm along with ~3-fold quenching at 537 nm. Similarly, upon gradual addition of **RhB** to the solution of **B2**, the intensity of the newly appeared peak at 585 nm increased gradually at different molar ratios, whereas the band at 519 nm experienced emission quenching upon excitation at 421 nm. In contrast, under similar conditions, **RhB** alone was found to be non-emissive upon excitation at 428 and 421 nm, eliminating the possibility of direct excitation of RhB. Additionally, the gel state of **B2** (**GB_2**) is utilised for the construction of ALHSs (Fig. S36, ESI†). With the gradual increase in the molar ratio of RhB from 250 : 1 to 27 : 1 (**GB_2** : **RhB**), the fluorescence intensity of **GB_2** at 515 nm decreased notably whereas the fluorescence intensity of **RhB** at 577 nm increased remarkably under excitation at 430 nm.

Therefore, it can be safely concluded that an efficient FRET process exists between aggregates of **B1** and **B2** and gel **GB_2** with **RhB**; in these systems, AIEgen acts as the energy donor and **RhB** acts as the acceptor. Further, to obtain better insight into the energy transfer process, the fluorescence lifetime of the donor was measured in the presence of the acceptor. In this direction, fluorescence lifetime decay profiles for **B1**/**RhB** and **B2**/**RhB** at different ratios are investigated in an aqueous medium (f_w = 90%) at 537, 583 nm and 520, 585 nm, respectively. Notably, luminophore **B1** (τ_{agg} = 0.87 ns) showed a higher fluorescence lifetime relative to **B1** in the presence of **RhB** (D : A = 27 : 1) (τ = 0.37 ns) (Fig. 7). Further, the fluorescence

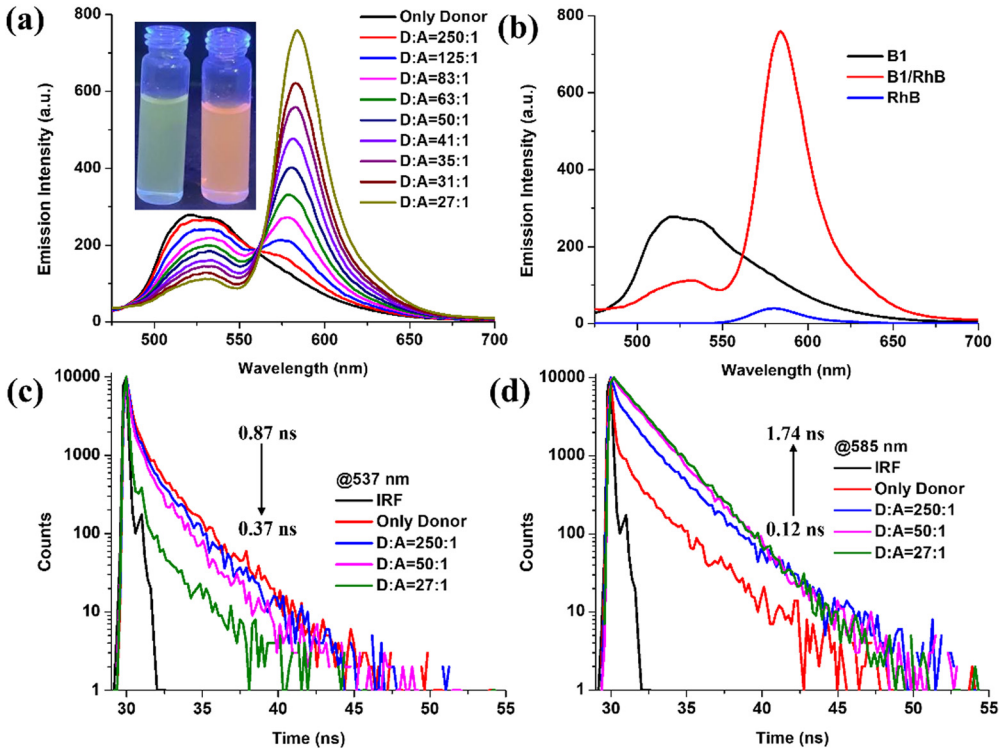

Fig. 7 Fluorescence spectra of **B1** (*c*, 5.0 × 10^{-5} M) with gradual addition of RhB (λ_{ex} = 421 nm) in THF/water (f_w 90%) (*c*, 0.0, 0.2 × 10^{-6}, 0.4 × 10^{-6}, 0.6 × 10^{-6}, 0.8 × 10^{-6}, 1.0 × 10^{-6}, 1.2 × 10^{-6}, 1.4 × 10^{-6}, 1.6 × 10^{-6}, and 1.8 × 10^{-6} M); (b) emission spectra of **B1** (*c*, 5.0 × 10^{-5} M), RhB + **B1** (*c*, 5.0 × 10^{-5} M, [RhB] *c*, 1.0 × 10^{-4} M) and RhB (*c*, 2.5 × 10^{-5} M). (c) and (d) Change in the fluorescence decay profiles of **B1** in the presence of RhB in THF/water (90%; v/v).

lifetime of the self-assembly of **B2** and **RhB** (τ = 0.11 ns) were found to be shorter (Fig. S35, ESI†) than the fluorescence lifetime of **B2** (τ_{agg} = 0.22 ns) at a similar molar ratio (D : A = 27 : 1). Simultaneously, **RhB** showed enhanced fluorescence lifetimes of 1.74 (**B1**) and 1.82 ns (**B2**) upon excitation at 428 and 421 nm. Additionally, the **GB_2/RhB** dyad showed similar fluorescence lifetime results in the gel state. The decay profile of **GB_2** monitored at 515 nm steadily decreased from 0.10 to 0.08 ns along with an increase in lifetime from 0.09 to 3.56 ns of **RhB** at 577 nm (Fig. S36, ESI†). Such a decrease in fluorescence lifetime suggests an energy transfer from donor to acceptor moieties. The energy transfer efficiency and antenna effect for BODIHYs are calculated in the aggregated state (**B1** = 58%, 16.4; **B2** = 3.4%, 15.6) and gel state (**GB_2** = 26%, 4.4) at a ratio of 27 : 1 (ESI†). These results indicate that energy transfer can occur from the AIEgens (**B1** and **B2**) to the **RhB** in aggregated and gel states. Thus, we conclude that successful FRET may be responsible for the observed sensitization of **RhB** by **B1** and **B2**. Notably, this antenna effect is similar to the recently reported values for other artificial light-harvesting systems in aqueous and organic environments.

Conclusion

In conclusion, two BODIHYs (**B1** and **B2**) and their corresponding ligands (**L1** and **L2**) are designed, synthesized and thoroughly characterized. With the intent of creating gel *via* saponification, several ester substituents ($-COOC_2H_5$) on the phenyl rings of **L1–L2** and **B1–B2** are introduced, further leading to the construction of supramolecular gels **GL_2** and **GB_2** based on **L2** and **B2**, respectively. The presence of two peripheral ester groups on the benzene rings of **L2** and **B2**, in contrast to those on **L1** and **B1**, enables strong gelation due to increased π–π interaction in the former following hydrolysis under basic conditions. The ligands and BODIHYs display good emission in the solution and solid states. **B1** and **B2** showed excellent AIE behaviour with ∼5- and 8-fold emission enhancement in the aggregated state, respectively. RIR is the driving force behind the AIE activity, as established through viscosity experiments. A comparative account of optical behaviour in solution and aggregated states is provided through the evaluation of intermolecular interactions visualized through single-crystal XRD data. **B1**, **B2** and **GB_2** have further been utilized for fabrication of ALHSs: **B1**/RhB, **B2**/RhB and **GB_2**/RhB. The energy transfer efficiency and antenna effect for BODIHYs are **B1** = 58%, 16.4; and **B2** = 3.4%, 15.6 in the aggregated state and **GB_2** = 26%, 4.4 in the gel state at a ratio of 27 : 1. Thus, the present work relays the pioneering work in supramolecular gelation of BODIHYs and exploration of those gels for constructing ALHSs. This will enable further exploration of the outstanding optical properties of BODIHYs for the fabrication of novel and more efficient ALHSs.

Data availability

This is to certify that all the data related to the present work have been provided in figures and tables in the manuscript and its ESI.† Crystallographic data have been provided in separate checkCIF files.

Conflicts of interest

There are no conflicts to declare.

Acknowledgements

Authors gratefully acknowledge the Science and Engineering Research Board (SERB), New Delhi, India (Scheme ECR/2018/001810) and BHU IOE cell (Seed/Incentive Grant) for providing financial assistance and also to CSIR, New Delhi, India for award of a Senior Research Fellowship to Durgendra Yadav (09/0013(11822)/2021-EMR-I). We are thankful to the Head, Departments of Chemistry, Institute of Science, Banaras Hindu University, Varanasi (UP) India, for extending laboratory facilities. We are also thankful to Dr Mrigendra Dubey, Soft Materials Research Laboratory, Department of Metallurgy Engineering and Materials Science, IIT Indore, India and to Dr Avanish Singh Parmar, Biophysics and Nanotechnology Laboratory, Department of Physics, IIT (BHU) Varanasi, India for providing rheology data.

References

1 K. K. Jaiswal, C. R. Chowdhury, D. Yadav, R. Verma, S. Dutta, K. S. Jaiswal, B. Sangmesh and K. S. K. Karuppasamy, *Energy Nexus*, 2022, **7**(100118), 2772–4271.
2 N. Gallandat, J. Bérard, F. Abbetab and A. Züttel, *Sustainable Energy Fuels*, 2017, **1**, 1748–1758.
3 D. Gielen, F. Boshell, D. Saygin, M. D. Bazilian, N. Wagner and R. Gorini, *Energy Strategy Rev.*, 2019, **24**, 38–50.
4 P. J. Megía, A. J. Vizcaíno, J. A. Calles and A. Carrero, *Energy Fuels*, 2021, **35**(20), 16403–16415.
5 K. Alper, K. Tekin, S. Karagöz and A. J. Ragauskas, *Sustainable Energy Fuels*, 2020, **4**, 4390–4414.
6 C. J. Quarton, O. Tlili, L. Welder, C. Mansilla, H. Blanco, H. Heinrichs, J. Leaver, N. J. Samsatli, P. Lucchese, M. Robiniusc and S. Samsatli, *Sustainable Energy Fuels*, 2020, **4**, 80–95.
7 J. Lv, J. Xie, A. G. A. Mohamed, X. Zhang, Y. Feng, L. Jiao, E. Zhou, D. Yuan and Y. Wang, *Nat. Rev. Chem.*, 2023, **7**, 91–105.
8 J. Barber, *Chem. Soc. Rev.*, 2009, **38**, 185–196.
9 M. M. Hasan, S. Hossain, M. Mofijur, Z. Kabir, I. A. Badruddin, T. M. Y. Khan and E. Jassim, *Energies*, 2023, **16**(18), 6456.
10 R. Vargas, D. Carvajal, L. Madriz and B. R. Scharifker, *Energy Rep.*, 2020, **6**(4), 2–12.
11 T. Kawawaki, Y. Mori, K. Wakamatsu, S. Ozaki, M. Kawachi, S. Hossain and Y. Negishi, *J. Mater. Chem. A*, 2020, **8**, 16081–16113.
12 Z. Lian, Y. Kobayashi, J. J. M. Vequizo, C. S. K. Ranasinghe, A. Yamakata, T. Nagai, K. Kimoto, K. Kobayashi, K. Tanaka,

T. Teranishi and M. Sakamoto, *Nat. Sustain.*, 2022, **5**, 1092–1099.
13 R. P. Steer, *Dalton Trans.*, 2018, **47**, 8517–8525.
14 Y. Wang, N. Han, X. Li, S. Yu and L. Xing, *Chem. Phys. Mater.*, 2022, **1**, 281–293.
15 X. Feng, X. Ding, L. Chen, Y. Wu, L. Liu, M. Addicoat, S. Irle, Y. Dong and D. Jiang, *Sci. Rep.*, 2016, **6**, 32944.
16 Y. X. Hu, W. J. Li, P. P. Jia, X. Q. Wang, L. Xu and H. B. Yang, *Adv. Opt. Mater.*, 2020, **8**, 2000265.
17 F. Hajjaj, Z. S. Yoon, M. C. Yoon, J. Park, A. Satake, D. Kim and Y. Kobuke, *J. Am. Chem. Soc.*, 2006, **128**(14), 4612–4623.
18 W. J. Li, X. Q. Wang, W. Wang, Z. Hu, Y. Ke, H. Jiang, C. He, X. Wang, Y. X. Hu, P. P. Jia, P. Yin, J. Chen, H. Sun, Z. Sun, L. Xu and H. B. Yang, *Giant*, 2020, **2**, 100020.
19 W. J. Li, X. Q. Wang, D. Y. Zhang, Y. X. Hu, W. T. Xu, L. Xu, W. Wang and H. B. Yang, *Angew. Chem., Int. Ed.*, 2021, **60**, 18761–18768.
20 Y. Wang, Y. Lai, T. Ren, J. Tang, Y. Gao, Y. Geng, J. Zhang and X. Ma, *Langmuir*, 2023, **39**, 1103–1110.
21 Y. Wang, Y. Gao, J. Tang, T. Ren, J. Zhang, Y. Liang, J. Wei, E. Feng and X. Ma, *ACS Appl. Polym. Mater.*, 2023, **5**(5), 3809–3816.
22 X. Ma, J. Tang, T. Ren, J. Zhang, Y. Liang, J. Weia and E. Feng, *RSC Appl. Interfaces*, 2024, **1**, 215–221.
23 S. K. Bhaumik, D. Maity, I. Basu, S. Chakrabarty and S. Banerjee, *Chem. Sci.*, 2023, **14**, 4363–4374.
24 K. Trofymchuk, A. Reisch, P. Didier, F. Fras, P. Gilliot, Y. Mely and A. S. Klymchenko, *Nat. Photonics*, 2017, **11**, 657–663.
25 Y. X. Li, J. Li, H. B. Zeng, X. J. Zhang, S. Cosnier and D. Shan, *Anal. Chem.*, 2023, **95**(6), 3493–3498.
26 V. D. Singh, B. K. Dwivedi, Y. Kumar and D. S. Pandey, *New J. Chem.*, 2021, **45**, 1677–1685.
27 B. Shi, Y. Liu, H. Zhu, R. T. Vanderlinden, L. Shangguan, R. Ni, K. Acharyya, J. H. Tang, Z. Zhou, X. Li, F. Huang and P. J. Stang, *J. Am. Chem. Soc.*, 2019, **141**(16), 6494–6498.
28 A. Arrigo, G. L. Ganga, F. Nastasi, S. Serroni, A. Santoro, M. P. Santoni, M. Galletta, S. Campagna and F. Puntoriero, *C. R. Chimie*, 2017, **20**, 209–220.
29 H. Q. Peng, L. Y. Niu, Y. Z. Chen, L. Z. Wu, C. H. Tung and Q. Z. Yang, *Chem. Rev.*, 2015, **115**, 7502–7542.
30 K. E. Sapsford, L. Berti and I. L. Medintz, *Angew. Chem., Int. Ed.*, 2006, **45**, 4562–4588.
31 X. Ma, B. Qiao, J. Yue, Y. Geng, Y. Lai, J. Zhang, E. Feng, Z. Lia and X. Hana, *Mater. Adv.*, 2022, **3**, 4531–4535.
32 X. M. Chen, X. Chen, X. F. Hou, S. Zhang, D. Chen and Q. Li, *Nanoscale Adv.*, 2023, **5**, 1830–1852.
33 X. Ma, J. Yue, Y. Wang, Y. Gao, B. Qiao, E. Feng, Z. Li, F. Ye and X. Han, *Soft Matter*, 2021, **17**, 5666–5670.
34 P. Verma, A. Singh and T. K. Maji, *Chem. Sci.*, 2021, **12**, 2674–2682.
35 Y. Liang, K. Wang, J. Li, Y. Zhang, J. Liu, K. Zhang, Y. Cui, M. Wanga and C. S. Liu, *Mater. Horiz.*, 2022, **9**, 1700–1707.
36 D. K. Smith, *Soft Matter*, 2024, **20**, 10–70.
37 K. J. Skilling, F. Citossi, T. D. Bradshaw, M. Ashford, B. Kellama and M. Marlow, *Soft Matter*, 2014, **10**, 237–256.
38 D. M. Raymond, B. L. Abraham, T. Fujita, M. J. Watrous, E. S. Toriki, T. Takano and B. L. Nilsson, *ACS Appl. Bio Mater.*, 2019, **2**(5), 2116–2124.
39 K. Sugiyasu, M. Numata, N. Fujita, S. M. Park, Y. J. Yun, B. H. Kimb and S. Shinkai, *Chem. Commun.*, 2004, 1996–1997.
40 L. Huo, H. Zhang, Y. Wang, Y. Wang, B. Deng and L. Jin, *Colloids Surf., A*, 2022, **648**, 129197.
41 J. Raeburna and D. J. Adams, *Chem. Commun.*, 2015, **51**, 5170–5180.
42 B. O. Okesolaa and D. K. Smith, *Chem. Soc. Rev.*, 2016, **45**, 4226–4251.
43 E. J. Cho, I. Y. Jeong, S. J. Lee, W. S. Han, J. K. Kang and J. H. Jung, *Tetrahedron Lett.*, 2008, **6**, 1076–1079.
44 C. Zhu, R. T. K. Kwok, J. W. Y. Lam and B. Z. Tang, *ACS Appl. Bio Mater.*, 2018, **1**(6), 1768–1786.
45 Y. Hong, J. W. Y. Lama and B. Z. Tang, *Chem. Commun.*, 2009, 4332–4353.
46 Z. Li, X. Ji, H. Xie and B. Z. Tang, *Adv. Mater.*, 2021, **33**, 2100021.
47 A. Tran, M. Leroux, C. Michelin, F. Réveret, D. Boyer and F. Cisnetti, *J. Mater. Chem. C*, 2023, **11**, 14896–14905.
48 S. Leichnitz, K. C. Dissanayake, A. H. Winter and P. H. Seeberge, *Chem. Commun.*, 2022, **58**, 10556–10559.
49 D. A. Merkushev, S. D. Usoltsev, Y. S. Marfin, A. P. Pushkarev, D. Volyniuk, J. V. Grazulevicius and E. V. Rumyantsev, *Mater. Chem. Phys.*, 2017, **187**, 104–111.
50 Z. Liu, Z. Jiang, M. Yan and X. Wang, *Front. Chem.*, 2019, **7**, 712–727.
51 H. Qian, M. E. Cousins, E. H. Horak, A. Wakefield, M. D. Liptak and I. Aprahamian, *Nat. Chem.*, 2017, **9**, 83–87.
52 L. A. Tatum, X. Su and I. Aprahamian, *Acc. Chem. Res.*, 2014, **47**(7), 2141–2149.
53 X. Su and I. Aprahamian, *Chem. Soc. Rev.*, 2014, **43**, 1963–1981.
54 D. Cappello, A. E. R. Watson and J. B. Gilroy, *Macromol. Rapid Commun.*, 2021, **42**, 2000553.
55 D. Cappello, R. R. Maar, V. N. Staroverov and J. B. Gilroy, *Chem. – Eur. J.*, 2020, **26**, 5522–5529.
56 V. D. Singh, R. S. Singh, R. P. Paitandi, B. K. Dwivedi, B. Maiti and D. S. Pandey, *J. Phys. Chem. C*, 2018, **122**(9), 5178–5187.
57 A. Kumar, R. S. Singh, A. Kumar, A. Ali, A. Biswas and D. S. Pandey, *Chem. – Eur. J.*, 2016, **22**, 13799–13804.
58 P. Demare and I. Regla, *J. Chem. Educ.*, 2012, **89**(1), 147–149.
59 A. Kumar, M. Dubey, R. Pandey, R. K. Gupta, A. Kumar, A. C. Kalita and D. S. Pandey, *Inorg. Chem.*, 2014, **53**(10), 4944–4955.
60 A. Kumar, M. Dubey, A. Kumar and D. S. Pandey, *Chem. Commun.*, 2014, **50**, 10086–10089.
61 M. H. S. Marqvorsen, A. Brinkø and H. H. Jensen, *Carbohydr. Res.*, 2020, **487**, 107886.
62 V. D. Singh, B. K. Dwivedi, Y. Kumar and D. S. Pandey, *Dyes Pigm.*, 2021, **184**, 108812.
63 R. S. Singh, A. Kumar, S. Mukhopadhyay, G. Sharma, B. Koch and D. S. Pandey, *J. Phys. Chem. C*, 2016, **120**(39), 22605–22614.
64 A. Biswas and S. Bera, *Langmuir*, 2023, **39**, 2667–2675.
65 M. F. Zaini, I. A. Razak, M. Z. Anis and S. Arshad, *Acta Crystallogr.*, 2019, **75**, 58–63.
66 X. Ma, B. Qiao, J. Yue, J. Yu, Y. Geng, Y. Lai, E. Feng, X. Hana and M. Liu, *Soft Matter*, 2021, **17**, 7813–7816.

